PAPER

Tuning the band gap energy of Cu_xIn_yS for superior photothermocatalytic CO_2 conversion to C_2H_4†

Longlong Wang,[ab] Ruirui Wang,*[b] Shuang Wei,[b] Kexin Li,[b] Hasnain Nawaz,[b] Bin He,[b] Mengyue Li[b] and Ruixia Liu [ID] *[abc]

Photothermal catalysis significantly enhances the efficiency of photocatalytic CO_2 reduction, offering a promising strategy for accelerated CO_2 resource utilization. Herein, a series of Cu_xIn_yS photocatalysts were synthesized, exhibiting tunable band gap energy by varying the Cu/In/S atomic ratios for photothermocatalytic CO_2 conversion to C_2H_4. The typical $CuInS_2$ catalyst demonstrates a more negative conduction band, significantly enhancing the electron reduction ability and facilitating the multi-electron reduction of CO_2 to C_2H_4. Additionally, the abundant sulfur vacancies in $CuInS_2$ generate additional active sites, enhance charge separation efficiency, and consequently improve catalytic activity. The generation rate of ethylene reaches 45.7 μmol g^{-1} h^{-1} with a selectivity of 79.7%. This study provides a new avenue for producing ethylene in photothermal catalysis, as well as highlighting the superiorities of the $CuInS_2$ catalyst.

1 Introduction

The excessive use of fossil fuels has led to excessive emissions of carbon dioxide (CO_2) into the atmosphere, causing severe climate change.[1–4] Photocatalytic conversion of CO_2 into hydrocarbons, artificial photosynthesis based on H_2O as the electron transfer medium and proton source, is a technology with environmental sustainability values.[5] Nevertheless, the efficiency of traditional photocatalytic CO_2 reduction remains hindered by the sluggish multi-electron transfer kinetics and suboptimal photon utilization efficiency.[6] Recent research reveals that the photothermal synergistic catalysis strategy can accelerate the photocatalytic conversion of CO_2, significantly enhancing the efficiency of CO_2 conversion and product selectivity.[7,8]

Photocatalytic efficiency of CO_2 conversion remains unsatisfactory, primarily because of the high thermodynamic stability of CO_2 molecules (ΔG 298 K^0 = −394.36 kJ mol^{-1})[9] and

a Henan Institute of Advanced Technology, Zhengzhou University, Zhengzhou, 450001, P. R. China
b Beijing Key Laboratory of Solid State Battery and Energy Storage Process, CAS Key Laboratory of Green Process and Engineering, State Key Laboratory of Mesoscience and Engineering, Institute of Process Engineering, Innovation Academy for Green Manufacture, CAS, Beijing 100190, P. R. China. E-mail: wangruirui@ipe.ac.cn, rxliu@ipe.ac.cn
c Longzihu New Energy Laboratory, Zhengzhou Institute of Emerging Industrial Technology, Henan University, Zhengzhou 450000, P. R. China
† Electronic supplementary information (ESI) available. See DOI: https://doi.org/10.1039/d5im00015g

the limited photon utilization.[10] To date, the primary products of CO_2 photothermal conversion have been C_1 compounds such as carbon monoxide, methane and formic acid.[11–14] C_2H_4, as an important C_2 chemical, has widespread applications in the synthesis of fibers, rubbers, plastics, and alcohols.[15] C–C coupling to produce C_2H_4 remains a significant challenge.[16] Theoretically, the selective photoreduction of CO_2 to C_2 products is primarily hindered by the difficulties associated with C–C coupling of key intermediates such as *CO and *COOH, which requires a high kinetic barrier.[17] To achieve efficient photothermal catalysis for the reduction of CO_2 to C_2H_4, the catalyst should possess several critical properties: efficient electron transfer and utilization, favorable adsorption of *CO intermediates,[18] and low energy barrier for the formation of *OCCO.[19,20] Accordingly, various catalytic strategies to enhance the photothermal catalytic CO_2 reduction capability have been investigated.

The band gap width is a pivotal factor influencing the performance of photocatalysts. Significant photogenerated electron–hole pairs can only be generated when the photon energy matches or exceeds the band gap energy. Concurrently, the conduction band (CB) potential must be more negative than the surface electron acceptor potential to ensure effective photocatalytic CO_2 reduction.[21] Bai *et al.*[22] synthesized a series of $Zn_mIn_2S_{3+m}$ catalysts with tailored bandgap energies and constructed $Zn_2In_2S_5/BiVO_4$ heterojunctions, which improve the separation of charge carriers and the photocatalytic performance. Chai *et al.*[23] synthesized various metal sulfides and demonstrated $CuInSnS_4$ as having the most negative

conduction band potential, achieving exceptional photocatalytic activity and selectivity for multi-electron CO_2 reduction. Therefore, tuning the band gap provides an effective strategy for enhancing the selectivity of photocatalytic CO_2 conversion to C_2H_4.

Metal sulfides have garnered extensive attention due to their structural tunability and broad light absorption capabilities.[24] Among these, Cu-based catalysts are highly efficient for CO_2 to C_2H_4 conversion due to their unique electronic structure and surface properties, which stabilize CO intermediates and promote C–C coupling.[25] Furthermore, In-based materials, as high-performance semiconductors, offer a favorable band structure for efficient electron–hole separation, enhancing photothermal catalytic performance. Gao et al.[26] reported $CuInP_2S_6$ nanosheets achieving 56.4% selectivity for the photocatalytic reduction of CO_2 to C_2H_4. The In sites facilitated the reduction of CO_2 to *CO, and the C–C coupling reaction occurred on the Cu sites. Furthermore, sulfur vacancies are frequently employed as a modulation strategy in metal sulfides. These defects significantly influence catalyst reactivity, modulate the electronic structure, facilitate charge transport, and effectively lower the kinetic barrier.[27,28] Yan et al.[29] designed a $Bi_2S_3@In_2S_3$ catalyst, with the In–S_v–Bi active center composed of adjacent Bi and In sites accompanied by abundant S_v defects, which reduces the energy barrier of CO_2 activation and C–C coupling, achieving a C_2H_4 generation rate of 11.81 $\mu mol\ g^{-1}\ h^{-1}$, with a selectivity of approximately 90%. Therefore, regulating the band structure and defect sites of the Cu_xIn_yS photocatalyst holds significant prospects for enhancing the reduction of CO_2 to C_2H_4.

Herein, we have successfully synthesized a series of metal sulfides, including $CuInS_2$, $CuIn_2S_4$, $CuIn_5S_8$, CuS and In_2S_3 by a simple hydrothermal method. Among these, the $CuInS_2$ catalyst demonstrated superior performance in photothermal catalytic CO_2 reduction, utilizing H_2O as a proton donor. The generation rate of ethylene reached 45.7 $\mu mol\ g^{-1}\ h^{-1}$ with a selectivity of 79.7%. The high performance was attributed to the photothermal effect, the high amount of sulfur vacancies and the narrow band gap of the $CuInS_2$ catalyst, where the abundant sulfur vacancies create additional active sites, promoting CO_2 activation, and a more negative conduction band significantly enhancing the electron reduction ability and facilitating the selectivity of CO_2 conversion to C_2H_4.

2 Results and discussion

X-ray diffraction (XRD) analysis was conducted to investigate the crystal structures and compositions of the synthesized samples.[30] As illustrated in Fig. 1a, the diffraction peaks observed at 27.9°, 46.5°, and 55.1° correspond to the (112), (220), and (312) crystal planes of the $CuInS_2$ phase, respectively. Additionally, diffraction peaks at 14.3°, 27.7°, 33.5°, 44.0°, and 48.1° are attributable to the (111), (311), (400), (511), and (440) crystal planes of $CuIn_2S_4$ and $CuIn_5S_8$ phases, respectively. In Fig. 1b, the XRD patterns further reveal the successful synthesis of monometallic sulfides, specifically CuS (PDF#79-2321) and In_2S_3 (PDF#73-1366). The diffraction peaks at 29.3°, 31.8°, 32.9°, 48.0°, 52.8°, and 59.4° are assigned to the (102), (103), (006), (110), (108), and (116) crystal planes of CuS, respectively. Meanwhile, peaks at 14.2°, 27.4°, 33.2°, 43.6°, and 47.7° correspond to the (103), (109), (00 12), (309), and (22 12) crystal planes of In_2S_3, respectively.

The microstructure and structural characteristics of the samples were carefully studied using scanning electron microscopy (SEM). The SEM comparisons of different samples under identical magnifications are shown in Fig. 2a–e. CuS exhibits a basic nanoparticle morphology, whereas $CuIn_2S_4$, $CuIn_5S_8$, In_2S_3 and $CuInS_2$ display a microsphere morphology self-assembled by nanosheets. The thicknesses of the catalyst flakes for CuS, $CuIn_2S_4$, $CuIn_5S_8$, In_2S_3 and $CuInS_2$ were measured to be 53 nm, 26 nm, 25 nm, 38 nm, and 20 nm, respectively. Notably, $CuInS_2$ demonstrates an ultrathin nanosheet morphology offering significant advantages for photocatalytic applications. The reduced thickness effectively shortens the charge transport distance, thereby minimizing the probability of charge recombination, ultimately enhancing the quantum efficiency of the photocatalytic process.[31]
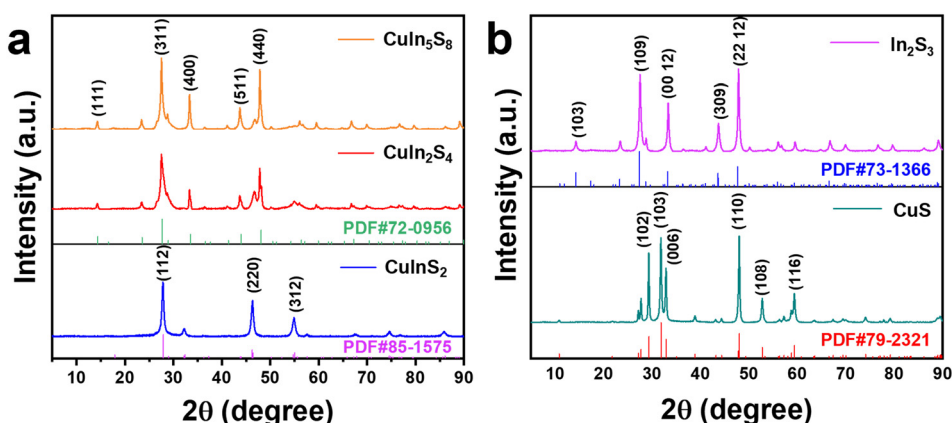

Fig. 1 (a) XRD patterns of $CuInS_2$, $CuIn_2S_4$ and $CuIn_5S_8$ samples; (b) XRD patterns of CuS and In_2S_3 samples.
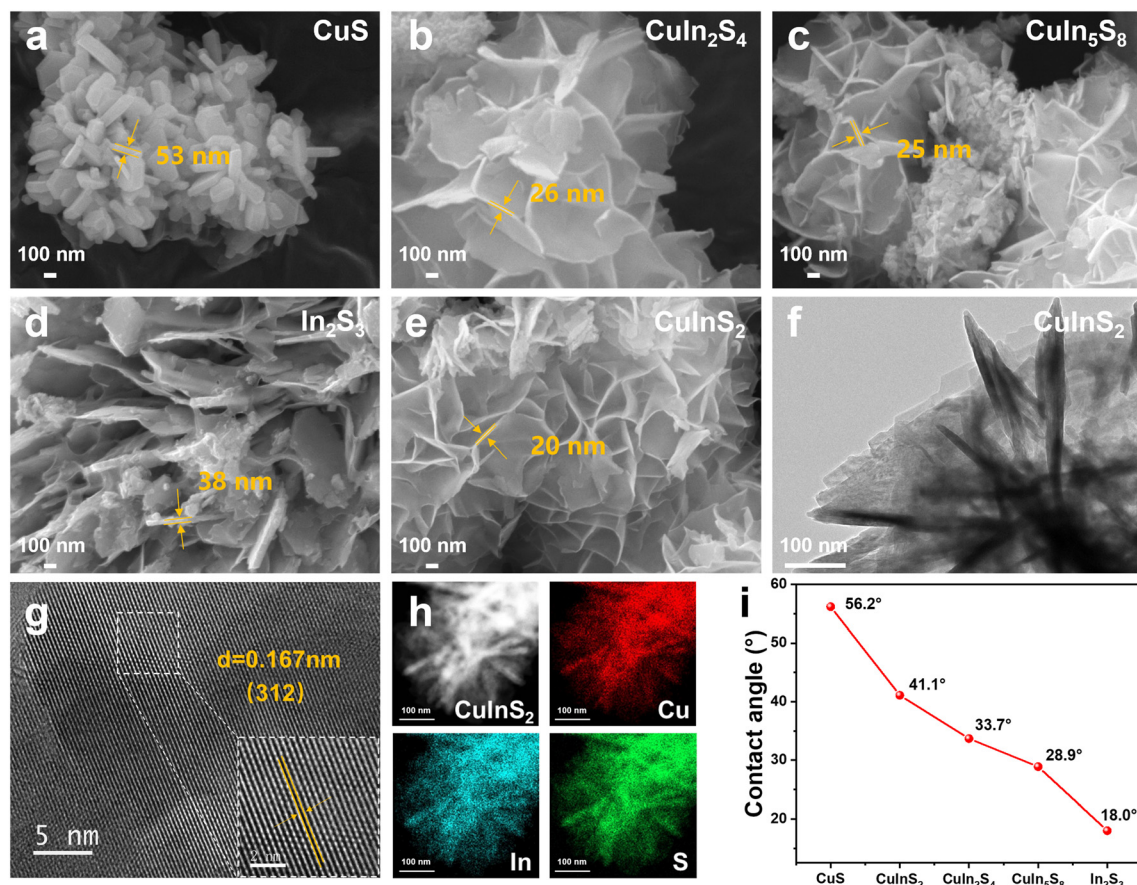
Fig. 2 SEM images of (a) CuS, (b) $CuIn_2S_4$, (c) $CuIn_5S_8$, (d) In_2S_3 and (e) $CuInS_2$; (f) TEM image, (g) HRTEM image, and (h) EDS mapping of $CuInS_2$; (i) static water contact-angle of Cu_xIn_yS.

The TEM analysis confirms that $CuInS_2$ consists of nanoflakes (Fig. 2f). Due to the low surface activity of $CuInS_2$ nanosheets, it is easy to agglomerate together, which forms the microsphere morphology observed in the SEM diagram. The high-resolution TEM image (Fig. 2g) reveals an exposed crystal plane of $CuInS_2$ with a lattice spacing of 0.167 nm, which corresponds to the (312) crystal face. Additionally, the elemental mapping in Fig. 2h demonstrates a uniform distribution of Cu, In, and S elements across the $CuInS_2$ nanoparticles. The composition of the $CuInS_2$ sample was analyzed by energy dispersive spectroscopy (EDS), as presented in Table S1.† The EDS results indicate that the atomic ratio of Cu, In and S is approximately 1:1:2, closely matching the stoichiometric composition of the $CuInS_2$ compound, indicating the high purity of the $CuInS_2$ nanocrystal. Furthermore, inductively coupled plasma mass spectrometry (ICP-MS) was employed to determine the metal element content in the $CuInS_2$ sample, with the results detailed in Table S2.† The Cu and In atomic ratio was found to be approximately 1:1, corroborating the theoretical stoichiometric value of $CuInS_2$. Collectively, these results confirm the successful preparation of the $CuInS_2$ nanocrystal with high-quality exposed (312) crystal faces. The hydrophilicity and hydrophobicity of the catalyst were examined, as depicted in Fig. 2i, and all the samples demonstrated hydrophilic characteristics, with contact angle measurements following the order: $CuS > CuInS_2 > CuIn_2S_4 > CuIn_5S_8 > In_2S_3$. This implies that a certain degree of hydrophilicity is beneficial to the adsorption of water on their surfaces, hence possibly aiding subsequent proton transfer to participate in the CO_2 reduction reactions.[32]

X-ray photoelectron spectroscopy (XPS) was employed to investigate the electronic states of the synthesized samples.[30] The high-resolution XPS spectra (Fig. 3a) reveal that the Cu $2p_{1/2}$ and Cu $2p_{3/2}$ binding energies for the $CuInS_2$ sample are 951.6 eV and 931.8 eV, respectively. Importantly, the Cu 2p binding energy of $CuInS_2$ is 0.3 eV lower than that observed for CuS. This shift can be attributed to changes in electron distribution and chemical bond strength arising from the interaction between Cu and In, resulting in a reduction in binding energy.[33] Further analysis of the In 3d region (Fig. 3b) shows that the binding energies of In $3d_{3/2}$ and In $3d_{5/2}$ in the $CuInS_2$ sample are 452.1 eV and 444.6 eV, respectively. Compared with In_2S_3, the In 3d binding energies of $CuInS_2$ uniformly shift to lower binding energy. This shift is attributed to the distinct coordination environments of In atoms in $CuInS_2$ and In_2S_3 because the partial In atom in In_2S_3 exists in the state of $[InS_4]$ tetrahedron.[34] For S 2p, the
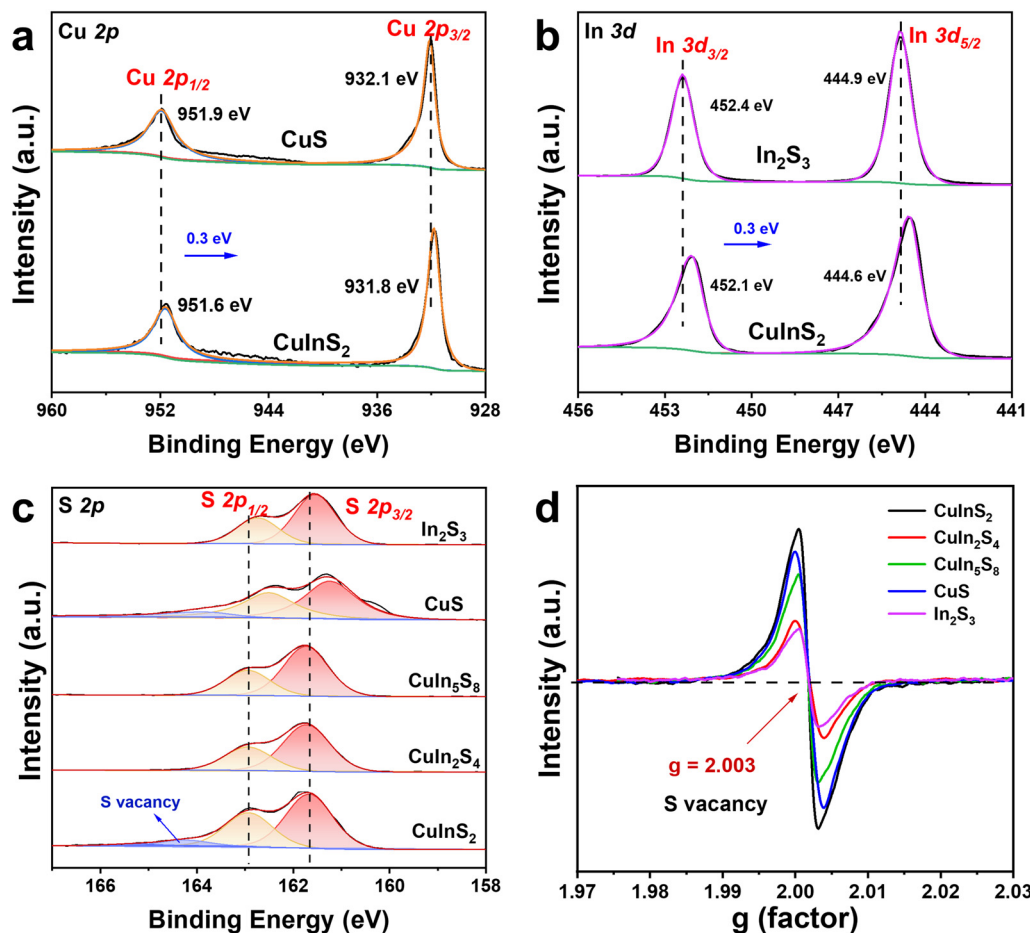
Fig. 3 XPS spectra of Cu_xIn_yS: (a) Cu 2p, (b) In 3d and (c) S 2p; (d) EPR spectra of Cu_xIn_yS.

binding energies of S $2p_{1/2}$ and S $2p_{3/2}$ are measured at 162.9 eV and 161.7 eV, respectively (Fig. 3c). Due to the fact that the average bond length between sulfur and metal atoms in $CuInS_2$ is slightly longer than that of monometallic sulfides, the S atom in $CuInS_2$ exhibits the highest binding energy. Notably, an additional peak at 164.5 eV is observed in both $CuInS_2$ and CuS samples, which has been attributed to sulfur vacancies as reported in the literature.[35] The higher binding energy of S atoms in $CuInS_2$ relative to monometallic sulfides suggests that the S atoms in $CuInS_2$ exist in an electron-deficient state. To provide further insights into the formation of sulfur vacancies, the $g = 2.003$ signal observed in the room-temperature EPR spectra was attributed to sulfur defects (Fig. 3d).[36] The presence of the sulfur vacancy has the potential to act as a reaction site to enhance the ability of CO_2 adsorption and subsequent activation and promote C–C coupling to generate C_2H_4.[23,29] Subsequent photo-thermal catalytic CO_2 reduction experiments also confirmed that the catalytic activity is positively correlated with the sulfur vacancy content, with $CuInS_2$, which has the highest sulfur vacancy concentration, exhibiting the best catalytic performance.

The photothermal catalytic performance of the sample for CO_2 reduction was evaluated using a flow fixed-bed reactor

(Fig. S1†). In this gas–solid reaction system, CO_2 and H_2O vapor were continuously introduced. Under illumination from a 300 W xenon lamp with full-spectrum output, the reaction temperature was maintained at 130 °C. After 6 hours of reaction, the only detectable gaseous products were C_2H_4 and CO, while no liquid-phase products were observed. To address the limitation of recombination of electron and hole pairs, triethanolamine (TEOA) was introduced as a sacrificial agent to effectively consume photogenerated holes formed during the photocatalytic reaction. To preliminarily exclude the impact of TEOA on the products of the CO_2 reduction reaction, its decomposition behavior was investigated under the N_2 atmosphere. As shown in Table S3,† at temperature of 130 °C, neither C_2H_4 nor CO was detected. Further, the thermal stability of TEOA was evaluated (Fig. S2†). Results show no mass loss at 130 °C, confirming the thermal stability of TEOA at this temperature. These findings collectively indicate that TEOA does not decompose to produce C_2H_4 or CO at the reaction temperature of 130 °C. Consequently, the influence of TEOA on the photothermal catalytic CO_2 reduction products can be preliminarily excluded.

The photothermal catalytic CO_2 reduction performance of the sample under reaction conditions of 0.5 MPa and 5 mL min^{-1} is shown in Fig. 4a. The $CuInS_2$ sample demonstrates
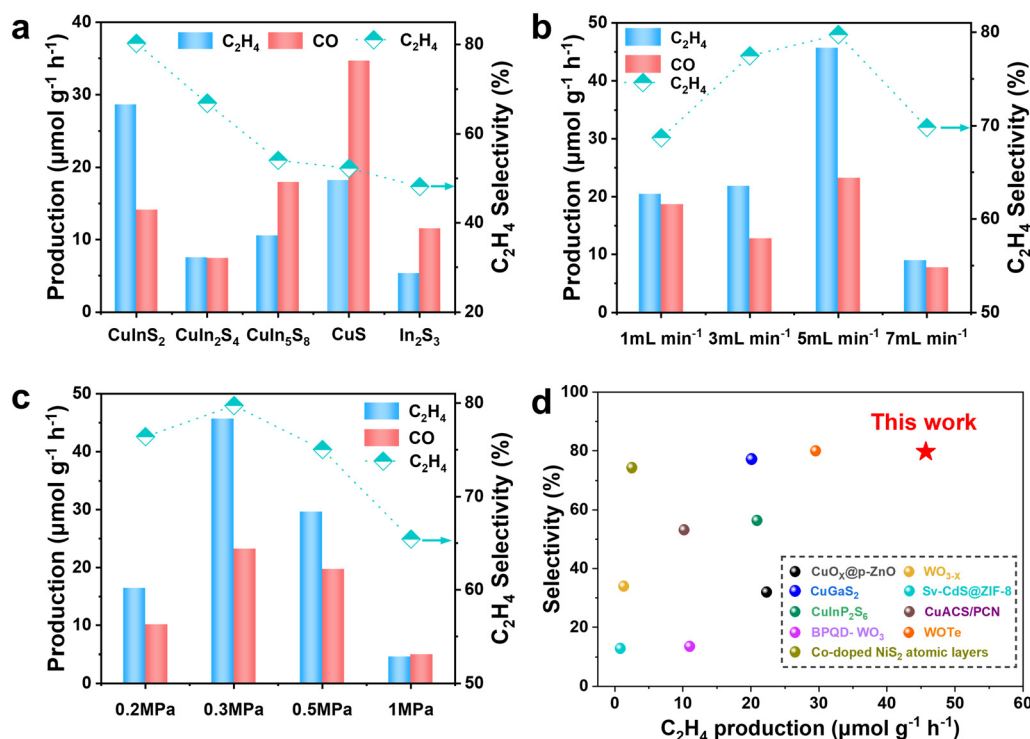
© 2025 The Author(s). Co-published by the Institute of Process Engineering, Chinese Academy of Sciences and the Royal Society of Chemistry

Ind. Chem. Mater., 2025, **3**, 440–451 | **443**

Fig. 4 (a) Photothermal catalytic CO_2 reduction performance of Cu_xIn_yS; photothermal catalytic CO_2 reduction performance of $CuInS_2$ catalysts (b) under different flow rates and (c) reaction pressures; (d) the C_2H_4 production rates and selectivity of different catalysts.

exceptional performance in photothermal catalytic CO_2 reduction, producing C_2H_4 and CO as the primary products. The generation rate of C_2H_4 was 28.6 μmol g^{-1} h^{-1}, while the CO generation rate was 14.1 μmol g^{-1} h^{-1}. The selectivity to C_2H_4 was calculated to be 80.2%, based on the carbon-containing product contents. In contrast, monometallic sulfides such as CuS and In_2S_3 predominantly produce CO as the main product. This variation in product selectivity suggests that bimetallic sulfides and monometallic sulfides differ in their CO_2 reduction mechanisms or exhibit distinct active sites.[23] Thermogravimetric analysis (Fig. S3†) was performed to investigate the thermal stability of the sample. The analysis reveals a degree of mass loss at approximately 130 °C, likely attributable to the presence of trace amounts of H_2O in the sample. As the temperature increases, the volatilization of H_2O results in the observed weight loss. The reaction conditions were further explored. The photothermal catalytic CO_2 reduction performance of the $CuInS_2$ sample under 0.3 MPa pressure and varying flow rates is evaluated in Fig. 4b, with superior photothermal catalytic performance demonstrated at a flow rate of 5 mL min^{-1}. This may be because the moderate flow rate enhances the supply of reactants, thereby increasing reaction rates, whereas excessive flow reduces catalyst interaction time, ultimately lowering efficiency.[37] The photothermal catalytic CO_2 reduction performance of the $CuInS_2$ sample under a flow rate of 5 mL min^{-1} and varying pressures is evaluated in Fig. 4c. The results demonstrate excellent photothermal catalytic performance at 0.3 MPa. Within a certain range, an increase

in pressure allows the active sites on the catalyst surface to interact more effectively with reactants, thereby improving catalyst activity.[37] Comparative analysis reveals that at a pressure of 0.3 MPa and a flow rate of 5 mL min^{-1}, the $CuInS_2$ sample exhibits optimal activity. Under these conditions, the rate of C_2H_4 generation reaches 45.7 μmol g^{-1} h^{-1}, with a C_2H_4 selectivity of 79.7%. Notably, compared with previously reported photothermal catalysts, the prepared $CuInS_2$ catalyst demonstrates superior rate and selectivity for C_2H_4 production (Fig. 4d, Table S4†).

With the increase in reaction time, the rates of C_2H_4 and CO exhibited a noticeable upward trend. Notably, after 6 hours of reaction, the rate of C_2H_4 using the $CuInS_2$ catalyst was significantly higher compared to the other samples (Fig. S4 and S5†). The durability and stability of the $CuInS_2$ catalyst were further assessed through cyclic experiments illustrated[38] in Fig. 5a, over five consecutive cycles (6 hours per cycle); the C_2H_4 production rate remained above 85% of the baseline activity, with the activity decay mainly attributed to catalyst poisoning by CO.[39–41] The XRD patterns of the $CuInS_2$ catalyst before and after the cyclic reaction (Fig. S6†) revealed no discernible changes in the crystal structure, confirming the structural integrity of the material post-reaction. Furthermore, the XPS results of the $CuInS_2$ catalyst after the reaction, shown in Fig. S7–S9,† indicated that the binding energies of Cu, In, and S in the sample remained relatively unchanged. These findings collectively suggest that the $CuInS_2$ catalyst maintains robust stability during the photothermal catalytic CO_2 reduction process. To confirm the
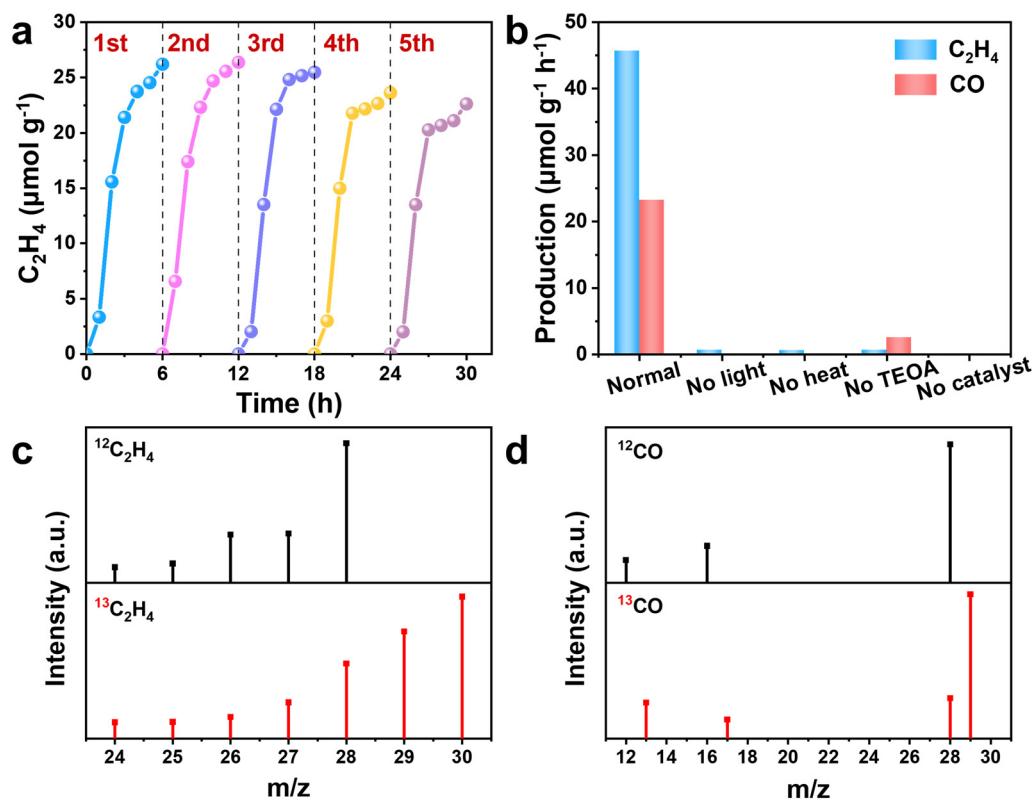
Fig. 5 (a) Stability test of CuInS$_2$; (b) control experiments of the CuInS$_2$ sample under different reaction conditions; GC–MS spectra of the produced (c) C$_2$H$_4$ and (d) CO from the photothermocatalytic reduction of ^{13}CO$_2$ or ^{12}CO$_2$ on CuInS$_2$.

occurrence of CO$_2$ reduction on CuInS$_2$, blank control experiments under various conditions were conducted. As shown in Fig. 5b, no product was detected in the absence of the catalyst, indicating its essential role in the reaction. When the reaction was performed at 130 °C without light, the rate of C$_2$H$_4$ generation was only 0.6 μmol g^{-1} h^{-1}, highlighting the fundamental importance of light as a driving force in the photothermal catalytic system. Similarly, under light irradiation but without external heating, the rate of C$_2$H$_4$ generation was merely 0.5 μmol g^{-1} h^{-1}. In contrast, under normal photothermal conditions (0.3 MPa, 5 mL min^{-1}, 130 °C, 300 W xenon lamp), the rate of C$_2$H$_4$ generation reached 45.7 μmol g^{-1} h^{-1}, demonstrating that thermal energy significantly enhances the production of C$_2$H$_4$.[42] The efficiency of photothermal conversion of CO$_2$ to C$_2$H$_4$ was notably higher than that achieved by photocatalysis or thermal catalysis alone. This underscores the indispensable roles of both light and heat in the photothermal reaction system. Importantly, the rate of C$_2$H$_4$ increased nearly tenfold upon the addition of the sacrificial agent TEOA. Control experiments conducted with N$_2$ instead of CO$_2$ yielded only trace amounts of C$_2$H$_4$ and CO (Table S5†), directly confirming that the source of the C$_2$H$_4$ and CO products was CO$_2$. To further verify the carbon source of C$_2$H$_4$ and CO in the products, isotope tracer experiments using ^{13}CO$_2$ were performed.[43] The products were analyzed by gas chromatography–mass spectrometry (GC–MS). As

shown in Fig. 5c and d, the mass spectral fragment ion distributions of C$_2$H$_4$ and CO were systematically characterized. The comparison experiments show that the fragment peaks of C$_2$H$_4$ (m/z = 28 → 30) and CO (m/z = 29 → 30) were obviously shifted when ^{13}CO$_2$ is involved in the reaction. This isotopic shift exclusively confirms that the carbon in C$_2$H$_4$ and CO originates from CO$_2$, rather than carbonaceous components of the catalyst or decomposition of organic sacrificial agents.

The light absorption capacity and charge separation efficiency of catalysts are critical factors influencing the experimental results of photothermal synergistic catalysis. The optical absorption abilities of the CuInS$_2$, CuIn$_2$S$_4$, CuIn$_5$S$_8$, CuS, and In$_2$S$_3$ samples were investigated using UV-vis diffuse reflectance spectroscopy (UV-vis DRS), as shown in Fig. S10.† Notably, the absorption edges of these materials are not distinct, reflecting full-spectrum absorption characteristics. The broad absorption range of these photocatalysts is advantageous for capturing photons, thereby enhancing photocatalytic reactions.[44] CuInS$_2$ exhibits strong light absorption across the spectral range, demonstrating promising potential for photocatalytic activity. Photoluminescence spectroscopy (PL) serves as an effective tool to assess the electron–hole recombination capability in photocatalysts. Lower recombination rates enhance charge utilization efficiency, thereby improving reactivity. As shown in Fig. 6a, the CuInS$_2$ sample exhibits the weakest PL signal,
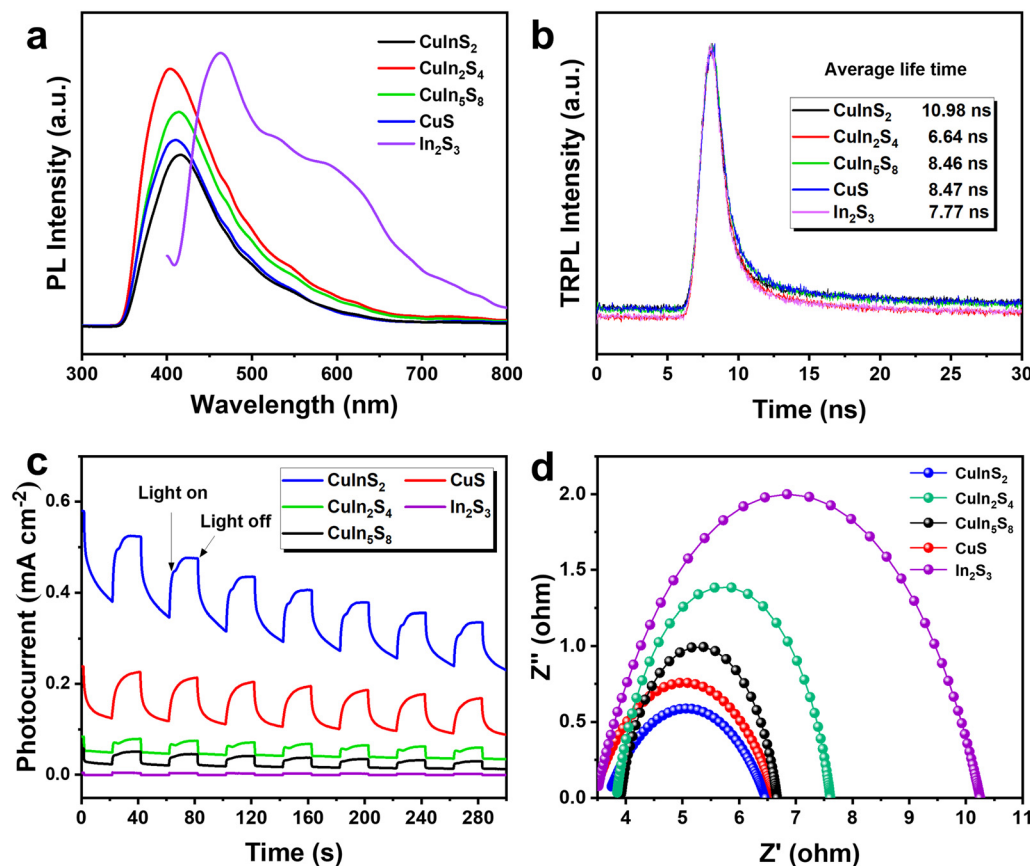
Fig. 6 (a) Steady-state fluorescence spectra, (b) transient fluorescence spectra, (c) transient photocurrent response curves and (d) electrochemical impedance spectra of Cu_xIn_yS.

indicative of the most effective charge separation. Furthermore, the time-resolved photoluminescence (TRPL) spectrum presented in Fig. 6b reveals that the $CuInS_2$ sample has an average carrier lifetime of 10.98 ns, which is markedly higher than that of the other samples. This extended carrier lifetime suggests a significant suppression of charge recombination. Additional photoelectrochemical tests corroborated these findings, further elucidating the electron–hole pair separation efficiency of the representative photocatalyst samples. These results underscore the importance of the $CuInS_2$ sample's superior charge separation characteristics in promoting photothermal synergistic catalysis.

Transient photocurrent measurements (Fig. 6c) were conducted to investigate the photocurrent response of the as-prepared samples under optical switching conditions. Among the tested samples, the $CuInS_2$ sample exhibited the highest photocurrent response, signifying superior separation efficiency of photogenerated electron–hole pairs under illumination conditions.[45,46] These results are consistent with previous studies. Electrochemical impedance spectroscopy (EIS) was employed to gain deeper insights into the electron transfer capabilities of the samples. As illustrated in Fig. 6d, the Nyquist plot for $CuInS_2$ demonstrates a smaller semicircle radius compared to the other samples, indicating

a lower charge transfer resistance and enhanced interfacial charge transfer efficiency.[47] Overall, these results suggest that $CuInS_2$ exhibits outstanding activity in photothermal catalytic CO_2 reduction reactions due to its excellent charge separation and electron transport properties.

To elucidate the factors governing the divergent selectivity patterns in catalytic reactions, we conducted a comprehensive analysis of the band gap properties for each candidate catalyst. The conduction band (CB) positions of the samples were evaluated through Mott–Schottky (M–S) analysis,[48] with CB potentials measured as −1.19 eV, −1.01 eV, −0.96 eV, −1.07 eV, and −0.74 eV (V $vs.$ NHE) for $CuInS_2$, $CuIn_2S_4$, $CuIn_5S_8$, CuS and In_2S_3, respectively (Fig. 7a–e). The positive slopes observed in the M–S curves at multiple frequencies (2000, 3000, and 4000 Hz) confirm that $CuInS_2$ is an n-type semiconductor. As revealed by XPS valence band spectra[49] (Fig. 7f), the valence band (VB) potentials were calculated to be 0.14 eV, 0.49 eV, 0.45 eV, 0.08 eV, and 1.64 eV (V $vs.$ NHE) for $CuInS_2$, $CuIn_2S_4$, $CuIn_5S_8$, CuS and In_2S_3, respectively. Based on the formula $E_g = E_{VB} - E_{CB}$,[44] the E_g values for $CuInS_2$, $CuIn_2S_4$, $CuIn_5S_8$, CuS and In_2S_3 were determined to be 1.33 eV, 1.50 eV, 1.41 eV, 1.15 eV, and 2.38 eV, respectively.

Based on the aforementioned results, an electronic band diagram relative to the standard hydrogen electrode was
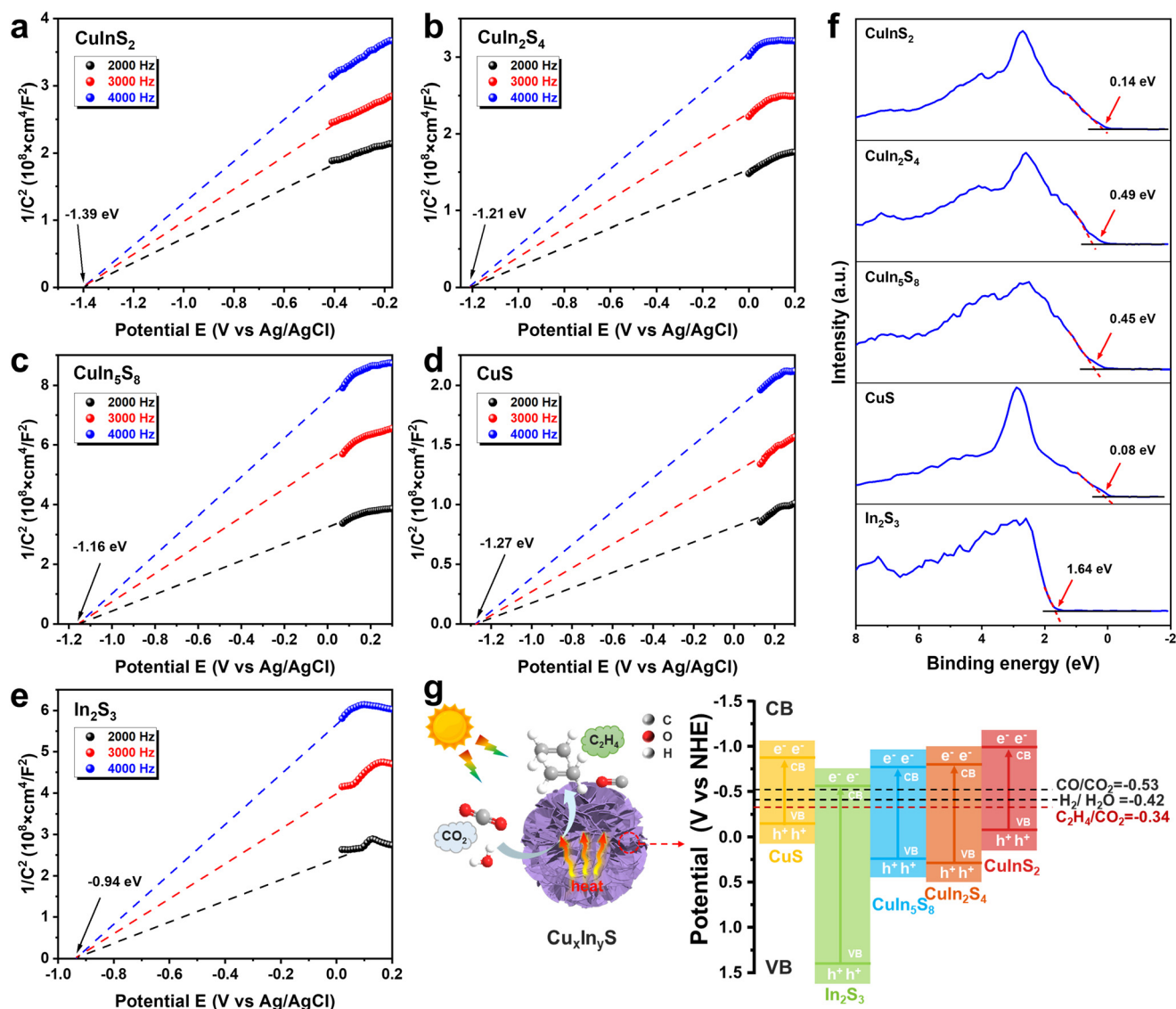
Fig. 7 Mott–Schottky curves of (a) $CuInS_2$, (b) $CuIn_2S_4$, (c) $CuIn_5S_8$, (d) CuS and (e) In_2S_3; (f) XPS valence band spectra of Cu_xIn_yS; (g) the optical band gap energy of Cu_xIn_yS.

constructed (Fig. 7g), which critically determine the driving force for redox reactions. All the samples demonstrated the capability to reduce CO_2 to C_2H_4 and CO. $CuInS_2$, in particular, has a band gap energy that aligns closely with the energy required for CO_2 reduction to C_2H_4, and its more negative CB position endows the electrons with stronger reducing power,[23] facilitating multi-electron CO_2 reduction pathways to C_2H_4. These findings underscore the potential of $CuInS_2$ as a highly efficient photocatalyst for CO_2 reduction, supported by its advantageous band structure and strong optical absorption properties.

To gain deeper insight into the band gap structure of Cu_x-In_yS, projected density of states (PDOS) calculations were performed using density functional theory (DFT),[50] as shown in Fig. 8. The results indicate that the band gap energies of CuS, $CuInS_2$ and In_2S_3 follow the order: CuS < $CuInS_2$ < In_2S_3. The band gap of $CuInS_2$ lies between that of CuS and

In_2S_3, enabling efficient visible-light absorption while avoiding the rapid carrier recombination caused by the excessively narrow band gap of CuS and the reduced light absorption efficiency resulting from the overly wide band gap of In_2S_3.[51] The PDOS for $CuInS_2$ reveals that the Cu 3d orbitals are the most active, contributing significantly to the electronic states near the Fermi level.[30] This suggests that during photoexcitation, electrons from the Cu 3p orbitals transition from the valence band maximum (VBM) to the conduction band minimum (CBM), playing a crucial role in the photocatalytic CO_2 reduction reaction.

3 Conclusion

In summary, this study has successfully synthesized a series of Cu_xIn_yS photocatalysts modulating the Cu/In/S atomic ratios by a simple hydrothermal method. The $CuInS_2$ catalyst
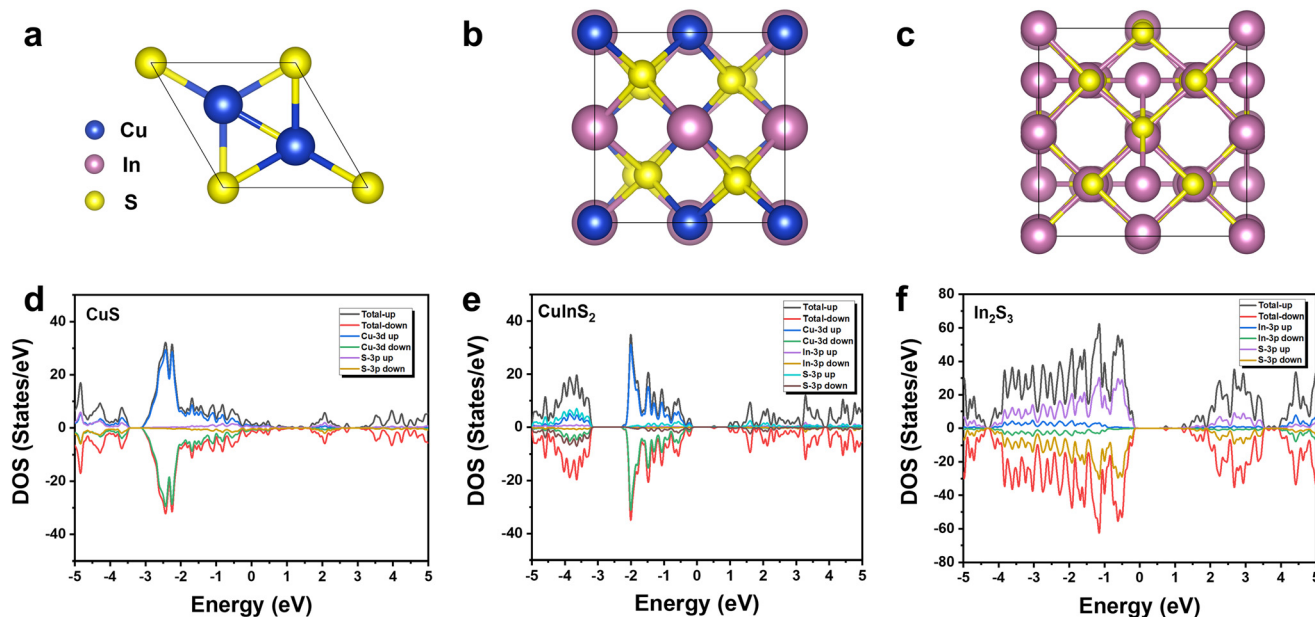
Fig. 8 Structural model diagram of (a) CuS, (b) CuInS$_2$ and (c) In$_2$S$_3$; PDOS of (d) CuS, (e) CuInS$_2$ and (f) In$_2$S$_3$.

demonstrated a remarkable rate of 45.7 μmol g^{-1} h^{-1} for photothermal CO$_2$ reduction with H$_2$O to C$_2$H$_4$, achieving a selectivity of 79.7% and excellent cycle stability. Control experiments conclusively proved the photothermal synergistic catalytic process, which significantly enhanced the efficiency of the reaction, addressing the limitations of single-mode photocatalysis and thermal catalysis. Electrochemical measurements, along with PL and TRPL analyses, confirmed the superior charge transport and separation efficiency demonstrated by the CuInS$_2$ catalyst. Furthermore, the abundant sulfur vacancies create additional active sites, promoting CO$_2$ activation, and the more negative conduction band of the CuInS$_2$ catalyst facilitates the reduction of CO$_2$ to C$_2$H$_4$. This work offers valuable insights into the design of metal sulfide catalysts for the photocatalytic conversion of CO$_2$ into C$_{2+}$ products.

4 Experimental section

4.1 Chemicals and materials

All chemicals were used as received without further purification. Cupric chloride dihydrate (CuCl$_2$·2H$_2$O), indium chloride tetrahydrate (InCl$_3$·4H$_2$O, 99.9%), thioacetamide (TAA, ≥98.0%), deionized water and anhydrous ethanol (C$_2$H$_5$OH, 99.5%) were purchased from Aladdin Reagent Company (Shanghai, China).

4.2 Preparation of CuInS$_2$

1.8 mmol of CuCl$_2$·2H$_2$O, 1.8 mmol of InCl$_3$·4H$_2$O and 3.6 mmol of TAA were dissolved in 80 mL deionized water and 80 mL ethanol, and reacted under hydrothermal conditions of 160 °C for 12 hours. After the reaction, the product was collected and washed with deionized water and ethanol, and

dried under vacuum at 60 °C for 12 hours; the synthesized sample was denoted as CuInS$_2$.

The synthesis methods for CuIn$_2$S$_4$ and CuIn$_5$S$_8$ are consistent with the described procedure, with the only modification being the variation in the molar ratios of CuCl$_2$·2H$_2$O, InCl$_3$·4H$_2$O, and TAA.

4.3 Preparation of CuS

1.8 mmol of CuCl$_2$·2H$_2$O and 3.6 mmol of TAA were dissolved in 80 mL deionized water and 80 mL ethanol, and reacted under hydrothermal conditions of 160 °C for 12 hours. After the reaction, the product was collected and washed with deionized water and ethanol, and dried under vacuum at 60 °C for 12 hours; the synthesized sample was denoted as CuS.

4.4 Preparation of In$_2$S$_3$

1.8 mmol of InCl$_3$·4H$_2$O and 3.6 mmol of TAA were dissolved in 80 mL deionized water and 80 mL ethanol, and reacted under hydrothermal conditions of 160 °C for 12 hours. After the reaction, the product was collected and washed with deionized water and ethanol, and dried under vacuum at 60 °C for 12 hours; the synthesized sample was denoted as In$_2$S$_3$.

4.5 Photothermal catalytic reduction of CO$_2$

For CO$_2$ photothermal conversion, 0.2 g catalyst and 0.1 mL TEOA were filled into the reaction tube. Subsequently, the flow fixed-bed reactor was filled with high-purity CO$_2$ gas to reach the reaction pressure. In the reaction system, deionized water was used as the proton source and a 300 W xenon lamp was used as the light source (Fig. S1†). The reaction products were analyzed in real time online by gas chromatography (GC 9790 II, FuLi, FID and TCD detector). The carbon-based

products of CO and C_2H_4 were quantified with a flame ionization detector (FID).

The photothermocatalytic CO and C_2H_4 production amounts and the rate could be calculated as follows:

$$Y = \frac{V}{22.4 \times 1000} \quad (1)$$

$$v = \frac{Y}{m \times t} \quad (2)$$

where Y represents CO and C_2H_4 production (μmol), V is the volume of CO and C_2H_4 (mL), v represents the CO and C_2H_4 production rate (μmol g^{-1} h^{-1}), m is the mass of sample (g), and t is the reaction time (h).

The selectivity for the CO_2 reduction products of CO and C_2H_4 was calculated using the following equation:

$$\text{CO selectivity (\%)} = \frac{n(\text{CO})}{n(\text{CO}) + 2n(C_2H_4)} \times 100\% \quad (3)$$

$$C_2H_4 \text{ selectivity (\%)} = \frac{2n(C_2H_4)}{n(\text{CO}) + 2n(C_2H_4)} \times 100\% \quad (4)$$

where $n(\text{CO})$ and $n(C_2H_4)$ are the molar yields of generated CO and C_2H_4 products, respectively.

4.6 Electrochemical measurements

The preparation of the working electrode was as follows. 5 mg photocatalyst was dispersed in a mixed solution of 350 μL C_3H_8O, 50 μL Nafion and 100 μL H_2O, and sonicated for 1 h. Then the mixed liquid was dispersed on FTO glass as a photoelectrode. The transient photocurrent response and electrochemical impedance spectra (EIS) were determined by using a CHI760E electrochemical workstation. 0.5 M Na_2SO_4 solution was used as the electrolyte and a 300 W xenon lamp was used as the light source. The sample photoelectrode, platinum foil and Ag/AgCl served as the working electrode, counter electrode and reference electrode, respectively.

4.7 Characterization

X-ray diffraction (XRD) was carried out using an X-ray diffractometer (Smartlab (9)) with the 2θ range from 5° to 90°. The morphology and sizes were examined by field-emission transmission electron microscopy (TEM) and field-emission scanning electron microscopy (SEM) using a JEOL F200 and JSM-7800 (Prime), respectively. X-ray photoelectron spectroscopy (XPS) analyzing the chemical compositions was conducted with an AXIS SUPRA+. The electron paramagnetic resonance (EPR) was measured on a Bruker EMX-Plus ESR spectrometer. The UV-vis diffuse reflectance spectra (DRS) were obtained with a Hitachi UH4150 spectrophotometer using $BaSO_4$ as the reflectance standard. Steady-state photoluminescence (PL) spectra of the as-prepared samples were detected with a Hitachi F-4700. Time-resolved photoluminescence (TRPL) spectra of the as-prepared samples were detected with an Edinburgh Instruments 980.

Data availability

The data that support the findings of this study are available from the corresponding author upon reasonable request.

Author contributions

Longlong Wang: investigation, confirmation, conceptualization, methodology, data analysis and writing – original draft. Ruirui Wang: supervision, formal analysis, data curation and writing – review & editing. Shuang Wei: investigation, confirmation, conceptualization. Kexin Li: methodology, data analysis. Hasnain Nawaz: conceptualization, methodology. Bin He: writing – review & editing. Mengyue Li: investigation. Ruixia Liu: supervision, resources, project administration, funding acquisition, writing – review & editing.

Conflicts of interest

The authors declare that they have no known competing financial interests or personal relationships that could have appeared to influence the work reported in this paper.

References

1 X. Li, J. Yu, M. Jaroniec and X. Chen, Cocatalysts for selective photoreduction of CO_2 into solar fuels, *Chem. Rev.*, 2019, **119**, 3962–4179.

2 P. Chen, P. Zhang, X. Kang, L. Zheng, G. Mo, R. Wu, J. Tai and B. Han, Efficient electrocatalytic reduction of CO_2 to ethane over nitrogen-doped Fe_2O_3, *J. Am. Chem. Soc.*, 2022, **144**, 14769–14777.

3 Y. Li, F. Li, A. Laaksonen, C. Wang, P. Cobden, P. Boden, Y. Liu, X. Zhang and X. Ji, Electrochemical CO_2 reduction with ionic liquids: Review and evaluation, *Ind. Chem. Mater.*, 2023, **1**, 410–430.

4 X. Jiao, Z. Hu, L. Li, Y. Wu, K. Zheng, Y. Sun and Y. Xie, Progress and perspectives for engineering and recognizing active sites of two-dimensional materials in CO_2 electroreduction, *Sci. China: Chem.*, 2022, **65**, 428–440.

5 L. Zhang, G. Kong, Y. Meng, J. Tian, L. Zhang, S. Wan, J. Lin and Y. Wang, Direct coupling of thermo and photocatalysis for conversion of CO_2-H_2O into fuels, *ChemSusChem*, 2017, **10**, 4709–4714.

6 Y. Zheng, L. L. Zhang, Y. K. Li, Y. Y. Wang, J. L. Chen, B. Z. Lin, Y. Z. Zheng, L. Cheng, S. B. Wang and Y. L. Chen, Triptycene incorporated carbon nitride based donor-acceptor

© 2025 The Author(s). Co-published by the Institute of Process Engineering, Chinese Academy of Sciences and the Royal Society of Chemistry

Ind. Chem. Mater., 2025, **3**, 440–451 | **449**

conjugated polymers with superior visible-light photocatalytic activities, *J. Colloid Interface Sci.*, 2022, **622**, 675–689.

7 M. Y. Sun, B. H. Zhao, F. P. Chen, C. B. Liu, S. Y. Lu, Y. F. Yu and B. Zhang, Thermally-assisted photocatalytic CO_2 reduction to fuels, *Chem. Eng. J.*, 2021, **408**, 127280.

8 D. Wu, K. Deng, B. Hu, Q. Lu, G. Liu and X. Hong, Plasmon-assisted photothermal catalysis of low-pressure CO_2 hydrogenation to methanol over Pd/ZnO catalyst, *ChemCatChem*, 2019, **11**, 1598–1601.

9 X. Chang, T. Wang and J. Gong, CO_2 photo-reduction: Insights into CO_2 activation and reaction on surfaces of photocatalysts, *Energy Environ. Sci.*, 2016, **9**, 2177–2196.

10 L. Xue, Q. Y. Fan, Y. Zhao, Y. Liu, H. Zhang, M. Sun, Y. Wang and S. Zeng, Ultralow Ag-assisted carbon-carbon coupling mechanism on Cu-based catalysts for electrocatalytic CO_2 reduction, *J. Energy Chem.*, 2023, **82**, 414–422.

11 S. Akrami, Y. Murakami, M. Watanabe, T. Ishihara, M. Arita, M. Fuji and K. Edalati, Defective high-entropy oxide photocatalyst with high activity for CO_2 conversion, *Appl. Catal., B*, 2022, **303**, 120896.

12 Q. Zhang, M. Mao, Y. Li, Y. Yang, H. Huang, Z. Jiang, Q. Hu, S. Wu and X. Zhao, Novel photoactivation promoted light-driven CO_2 reduction by CH_4 on Ni/CeO_2 nanocomposite with high light-to-fuel efficiency and enhanced stability, *Appl. Catal., B*, 2018, **239**, 555–564.

13 Y. Li, C. Wang, M. Song, D. Li, X. Zhang and Y. Liu, TiO_{2-x}/CoO_x photocatalyst sparkles in photothermocatalytic reduction of CO_2 with H_2O steam, *Appl. Catal., B*, 2019, **243**, 760–770.

14 J. Xiong, P. Song, J. Di and H. Li, Ultrathin structured photocatalysts: A versatile platform for CO_2 reduction, *Appl. Catal., B*, 2019, **256**, 117788.

15 M. H. Zhang and Y. Z. Yu, Dehydration of ethanol to ethylene, *Ind. Eng. Chem. Res.*, 2013, **52**, 9505–9514.

16 Q. Zhang, J. Wang, F. Guo, G. He, X. Yang, W. Li, J. Xu and Z. Yin, Nitrogen cold plasma treatment stabilizes Cu^0/Cu^+ electrocatalysts to enhance CO_2 to C_2 conversion, *J. Energy Chem.*, 2023, **84**, 321–328.

17 K. Das, R. Das, M. Riyaz, A. Parui, D. Bagchi, A. K. Singh, A. K. Singh, C. P. Vinod and S. C. Peter, Intrinsic charge polarization in $Bi_{19}S_{27}Cl_3$ nanorods promotes selective C-C coupling reaction during photoreduction of CO_2 to ethanol, *Adv. Mater.*, 2023, **35**, 2205994.

18 S. Rozas, F. C. Gennari, M. Atilhan, A. Bol and S. Aparicio, Theoretical investigation of carbon dioxide adsorption on MgH_2 with a cobalt catalyst, *Ind. Chem. Mater.*, 2024, **2**, 587–599.

19 H. Shi, H. Wang, Y. Zhou, J. Li, P. Zhai, X. Li, G. G. Gurzadyan, J. Hou, H. Yang and X. Guo, Atomically dispersed Indium-copper dual-metal active sites promoting C-C coupling for CO_2 photoreduction to ethanol, *Angew. Chem., Int. Ed.*, 2022, **134**, e202208904.

20 J. Albero, Y. Peng and H. García, Photocatalytic CO_2 reduction to C_{2+} products, *ACS Catal.*, 2020, **10**, 5734–5749.

21 B. Y. Lan and H. F. Shi, Review of systems for photocatalytic conversion of CO_2 to hydrocarbon fuels, *Acta Phys.-Chim. Sin.*, 2014, **30**, 2177–2196.

22 P. Bai, P. Wang, Y. Wu, X. Pang, M. Song, C. Du and Y. Su, Junction of $Zn_mIn_2S_{3+m}$ and bismuth vanadate as Z-scheme photocatalyst for enhanced hydrogen evolution activity: The role of interfacial interactions, *J. Colloid Interface Sci.*, 2022, **628**, 488–499.

23 Y. Chai, Y. Kong, M. Lin, W. Lin, J. Shen, J. Long, R. Yuan, W. Dai, X. Wang and Z. Zhang, Metal to non-metal sites of metallic sulfides switching products from CO to CH_4 for photocatalytic CO_2 reduction, *Nat. Commun.*, 2023, **14**, 6168.

24 Y. Chen, C. L. Tan, J. Y. Li, M. Y. Qi, Z. R. Tang and Y. J. Xu, Cocatalyst-modified In_2S_3 photocatalysts for C-N coupling of amines integrated with H_2 evolution, *Ind. Chem. Mater.*, 2024, **2**, 289–299.

25 S. You, J. Xiao, S. Liang, W. Xie, T. Zhang, M. Li, Z. Zhong, Q. Wang and H. He, Doping engineering of Cu-based catalysts for electrocatalytic CO_2 reduction to multi-carbon products, *Energy Environ. Sci.*, 2024, **17**, 5795–5818.

26 W. Gao, L. Shi, W. T. Hou, C. Ding, Q. Liu, R. Long, H. Q. Chi, Y. C. Zhang, X. Y. Xu, X. Y. Ma, Z. Tang, Y. Yang, X. Y. Wang, Q. Shen, Y. J. Xiong, J. L. Wang, Z. G. Zou and Y. Zhou, Tandem synergistic effect of Cu-In dual sites confined on the edge of monolayer $CuInP_2S_6$ toward selective photoreduction of CO_2 into multi-carbon solar fuels, *Angew. Chem., Int. Ed.*, 2024, **63**, e202317852.

27 X. Pan, M. Q. Yang, X. Fu, N. Zhang and Y. J. Xu, Defective TiO_2 with oxygen vacancies: Synthesis, properties and photocatalytic applications, *Nanoscale*, 2013, **5**, 3601–3614.

28 Y. Ji and Y. Luo, New mechanism for photocatalytic reduction of CO_2 on the anatase TiO_2(101) surface: The essential role of oxygen vacancy, *J. Am. Chem. Soc.*, 2016, **138**, 15896–15902.

29 K. Yan, D. Wu, T. Wang, C. Chen, S. Liu, Y. Hu, C. Gao, H. Chen and B. Li, Highly selective ethylene production from solar-driven CO_2 reduction on the Bi_2S_3@In_2S_3 catalyst with In-S_V-Bi active sites, *ACS Catal.*, 2023, **13**, 2302–2312.

30 J. Wang, C. Yang, L. Mao, X. Cai, Z. Geng, H. Zhang, J. Zhang, X. Tan, J. Ye and T. Yu, Regulating the metallic Cu-Ga bond by S vacancy for improved photocatalytic CO_2 reduction to C_2H_4, *Adv. Funct. Mater.*, 2023, **33**, 2213901.

31 C. Bie, J. Fu, B. Cheng and L. Zhang, Ultrathin CdS nanosheets with tunable thickness and efficient photocatalytic hydrogen generation, *Appl. Surf. Sci.*, 2018, **462**, 606–614.

32 J. R. Adleman, D. A. Boyd, D. G. Goodwin and D. Psaltis, Heterogenous catalysis mediated by plasmon heating, *Nano Lett.*, 2009, **9**, 4417–4423.

33 Z. Zhang, X. Ma, Y. Li, N. Ma, M. Wang, W. Liu, J. Peng, Y. Liu and Y. Li, Heterovalent metal pair sites on metal-organic framework ordered macropores for multimolecular Co-activation, *J. Am. Chem. Soc.*, 2024, **146**, 8425–8434.

34 F. Horani and E. Lifshitz, Unraveling the growth mechanism forming stable γ-In_2S_3 and β-In_2S_3 colloidal nanoplatelets, *Chem. Mater.*, 2019, **31**, 1784–1793.

35 L. Fan, S. Lei, H. M. K. Sari, L. Zhong, A. Kakimov, J. Wang, J. Chen, D. Liu, L. Huang, J. Hu, L. Lin and X. Li, Controllable S-vacancies of monolayered Mo-S nanocrystals for highly harvesting lithium storage, *Nano Energy*, 2020, **78**, 105235.

36 J. Wang, T. Bo, B. Shao, Y. Zhang, L. Jia, X. Tan, W. Zhou and T. Yu, Effect of S vacancy in Cu_3SnS_4 on high selectivity and activity of photocatalytic CO_2 reduction, *Appl. Catal., B*, 2021, **297**, 120498.

37 R. R. Ratnakar, S. Shankar, R. Agrawal and B. Dindoruk, Modeling and experimental study on CO_2 adsorption in fixed-bed columns: Applications to carbon capture and utilization, *J. Nat. Gas Sci. Eng.*, 2021, **94**, 104111.

38 C. Liao, Z. He, F. Wang, Y. Liu and L. Guo, Anti-site defect-induced cascaded sub-band transition in $CuInS_2$ enables infrared light-driven CO_2 reduction, *ACS Nano*, 2024, **18**, 35480–35489.

39 L. Falbo, C. G. Visconti, L. Lietti and J. Szanyi, The effect of CO on CO_2 methanation over Ru/Al_2O_3 catalysts: A combined steady-state reactivity and transient DRIFT spectroscopy study, *Appl. Catal., B*, 2019, **256**, 117791.

40 K. Sun, C. Shen, R. Zou and C. J. Liu, Highly active Pt/In_2O_3-ZrO_2 catalyst for CO_2 hydrogenation to methanol with enhanced CO tolerance: The effects of ZrO_2, *Appl. Catal., B*, 2023, **320**, 122018.

41 S. Xu, S. Chansai, S. Xu, C. E. Stere, Y. Jiao, S. Yang, C. Hardacre and X. Fan, CO poisoning of Ru catalysts in CO_2 hydrogenation under thermal and plasma conditions: A combined kinetic and diffuse reflectance infrared fourier transform spectroscopy-mass spectrometry study, *ACS Catal.*, 2020, **10**, 12828–12840.

42 X. Zhang, Y. Yang, Y. Hu, L. Xiong, T. Wang, P. Li and J. Shen, Photothermal catalytic C-C coupling to ethylene from CO_2 with high efficiency by synergistic cooperation of oxygen vacancy and half-metallic WTe_2, *J. Energy Chem.*, 2024, **93**, 547–556.

43 W. Wang, C. Deng, S. Xie, Y. Li, W. Zhang, H. Sheng, C. Chen and J. Zhao, Photocatalytic C-C coupling from carbon dioxide reduction on copper oxide with mixed-valence Copper(I)/Copper(II), *J. Am. Chem. Soc.*, 2021, **143**, 2984–2993.

44 W. Yang, G. Ma, Y. Fu, K. Peng, H. Yang, X. Zhan, W. Yang, L. Wang and H. Hou, Rationally designed Ti_3C_2 MXene@TiO_2/$CuInS_2$ Schottky/S-scheme integrated heterojunction for enhanced photocatalytic hydrogen evolution, *Chem. Eng. J.*, 2022, **429**, 132381.

45 N. Xiao, S. Li, X. Li, L. Ge, Y. Gao and N. Li, The roles and mechanism of cocatalysts in photocatalytic water splitting to produce hydrogen, *Chin. J. Catal.*, 2020, **41**, 642–671.

46 Y. Gao, G. Yang, Y. Dai, X. Li, J. Gao, N. Li, P. Qiu and L. Ge, Electrodeposited Co-substituted $LaFeO_3$ for enhancing the photoelectrochemical activity of $BiVO_4$, *ACS Appl. Mater. Interfaces*, 2020, **12**, 17364–17375.

47 Y. X. Pan, Y. You, S. Xin, Y. T. Li, G. T. Fu, Z. M. Cui, Y. L. Men, F. F. Cao, S. H. Yu and J. B. Goodenough, Photocatalytic CO_2 reduction by carbon-coated Indium-oxide nanobelts, *J. Am. Chem. Soc.*, 2017, **139**, 4123–4129.

48 Y. Sun, K. Lai, N. Li, Y. Gao and L. Ge, Efficient photocatalytic CO_2 reduction to CH_4 via electric field-regulated d-band center on Ga_2S_3/CuS S-type heterojunction interface structures, *Appl. Catal., B*, 2024, **357**, 124302.

49 X. Li, Y. Sun, J. Xu, Y. Shao, J. Wu, X. Xu, Y. Pan, H. Ju, J. Zhu and Y. Xie, Selective visible-light-driven photocatalytic CO_2 reduction to CH_4 mediated by atomically thin $CuIn_5S_8$ layers, *Nat. Energy*, 2019, **4**, 690–699.

50 T. Huang, Z. Huang, X. Yang, S. Yang, Q. Gao, X. Cai, Y. Liu, Y. Fang, S. Zhang and S. Zhang, Green and regulable synthesis of CdNCN on CdS semiconductor: Atomic-level heterostructures for enhanced photocatalytic hydrogen evolution, *Adv. Powder Mater.*, 2024, **3**, 100242.

51 D. Yang, Y. Li, R. Chen, X. Wang, Z. Li, T. Xing, L. Wei, S. Xu, P. Dai and M. Wu, Flower-like superstructure of boron carbon nitride nanosheets with adjustable band gaps for photocatalytic hydrogen peroxide production, *J. Mater. Sci. Technol.*, 2024, **183**, 23–31.

© 2025 The Author(s). Co-published by the Institute of Process Engineering, Chinese Academy of Sciences and the Royal Society of Chemistry

Ind. Chem. Mater., 2025, **3**, 440–451 | **451**